

Multifunctional Device for Circular to Linear Polarization Conversion and Absorption

Si-yuan Liao, Zhen Qiao, Jun-yang Sui, and Hai-feng Zhang*

In this paper, a metastructure multifunctional device for circular-to-linear polarization conversion (PC) and perfect absorption is proposed in which the electrical conductivity of the silicon material is controlled by light, thus changing the function of the device. The paper also explores three methods of optimizing bandwidth and their mechanisms, which are analyzed by means of current and energy density diagrams. The unit structure of this device adopts a 2×2 array, which is used for differentiated reflection of circular polarization waves, and forms linear polarization waves after reflection. In the other state, ultrawideband absorption can be achieved by changing the conductivity of silicon by external optical pumping, and the bandwidth is widened by inserting air resonators. In general, the device can form a PC at 0.89–1.31 THz with a relative bandwidth of 38% when there is no illumination. The resulting linear polarization wave has an axial ratio greater than 19 dB. When the silicon is excited by light resulting in a stable conductivity of around 9000 S m^{-1} , the absorption band is 0.89–2.01 THz, the relative bandwidth is 77%, and the absorption rate is above 90%. This device can be used for communication, electromagnetic cloaking, and modulation.

1. Introduction

As a kind of metamaterial with a 3D structure, metastructure has many excellent properties that traditional materials do not have. In the years since it was proposed, metastructures have been used in many fields, such as electromagnetic-induced transparency,^[1,2] perfect lens,^[3] frequency selective surface,^[4] and so on. Nowadays, due to the demand for device integration, multifunctional tunable devices have become a research hotspot. Common control means include light,^[5] pressure,^[6] thermal,^[7] electric field,^[8] etc. In the case of photocontrolled devices, photosensitive materials such as silicon, graphene, and liquid crystal are commonly used. Among them, silicon has the longest development history, low production cost, and mature preparation technology, and silicon has many advantages such as adjustable photoconductivity, high quantum efficiency, and stable


photoelectric performance.^[9] So far, many multifunctional devices have been proposed based on the above control methods. Zhang et al. designed an absorption-transmission multifunction device (MFD) based on graphene.^[10] Tang et al. used vanadium dioxide and graphene to realize tunable and switchable polarization conversion (PC).^[11] A PC metastructure based on shape memory alloy had been proposed by Wang et al.^[12]

Absorbers and polarization converters are two key applications in the field of metamaterials, which are already widely used in the field of communication and signal modulation. The perfect absorber was first proposed by Landy et al.^[13] in 2008 and can achieve close to 100% absorption of electromagnetic waves (EMWs) in the microwave band. Therefore, EMW absorbers are a good choice for electromagnetic shielding and stealth technology, or they can be used as switches.^[14–16]

In the field of communications, polarization converters are essential as electromagnetic waves of various polarization forms often need to be converted to each other due to environmental and channel constraints. The conversion between linear and linear polarization, circular and linear polarization, and circular and circular polarization are the three most common requirements,^[17] which help antennas to transmit or receive signals of different waveforms. Circular polarization (CP) waves, which are resistant to interference, are required due to rain and fog, while linear polarization (LP) wave antennas are also widely used in mobile communication systems due to their simplicity of implementation. For example, the Yagi antenna and Cone horn antenna are classical LP antennae and the equiangular spiral antenna is a typical CP antenna.^[18] For these reasons, circular-to-linear polarization converters have practical applications.

From the current research, it has been found that there is very little research work on combining absorbers and circular to linear polarization converters and that devices combining the two are equivalent to combining shielding and PC functions in one device and can facilitate device integration. This paper, therefore, proposes a light-controlled MFD that alters the photoconductivity of silicon with the aid of light, thereby enabling the transformation of absorption and circular to linear PC functions. When no light is applied, this MFD achieves a circular to linear PC function

S.-yuan Liao, Z. Qiao, J.-yang Sui, H.-feng Zhang
College of Electronic and Optical Engineering & College of Flexible
Electronics (Future Technology)
Nanjing University of Posts and Telecommunications
Nanjing 210023, P. R. China
E-mail: hanlor@njupt.edu.cn

 The ORCID identification number(s) for the author(s) of this article can be found under <https://doi.org/10.1002/andp.202300195>

DOI: 10.1002/andp.202300195

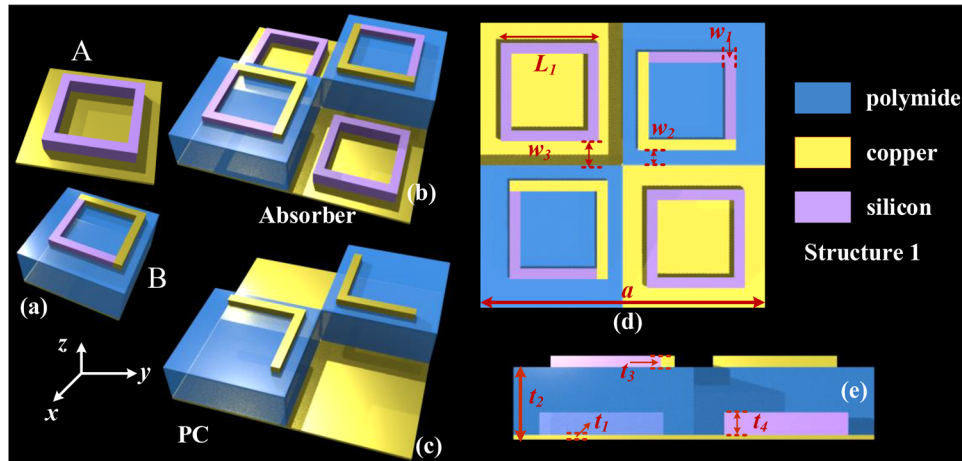


Figure 1. Schematic diagrams of the structure of the MFD: a) the two basic units A and B, b) the structure when operating as an absorber, c) the structure of the polarization converter, and d, e) top and side views of Structure 1 and dimensional parameters.

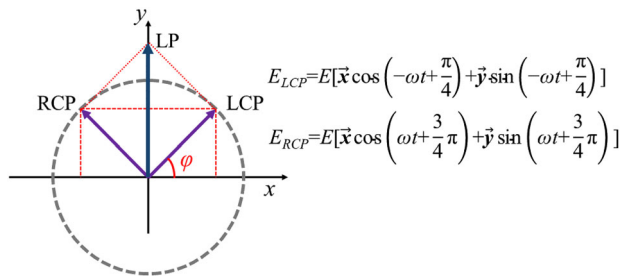


Figure 2. Schematic diagram of RCP and LCP waves synthesis.

in the range of 0.89–1.31 THz, with an output linear polarization wave with an axis ratio (AR) greater than 19 dB and a relative bandwidth (RB) of 38%. When the conductivity of the silicon is raised to 9000 S m^{-1} using light pumping, the MDF exhibits an absorption function, achieving over 90% absorption in the range of 0.89–2.01 THz, with an RB of 77%. The proposed device can be used in communication, signal modulation, electromagnetic pollution prevention, and other fields.

2. Design and Simulations

2.1. Theoretical Analysis and Simulation of the Initial Design

As shown in **Figure 1a**, the proposed MFD consists of two basic cells which together form the 2×2 array illustrated in **Figure 1b**, and such an array extended periodically constitutes the working device. As mentioned above, when the silicon is excited, the MFD has an absorption function, i.e., the structure in **Figure 1b**, while when the silicon is not excited, the PC function is mainly performed by copper folds, as demonstrated in **Figure 1c**. The specific dimensional parameters are given in **Figure 1d,e**, the exact values of which will be listed later, for Structure 1. The chosen material parameters are as follows: the conductivity of copper is $\sigma_{\text{Cu}} = 5.8 \times 10^7 \text{ S m}^{-1}$,^[19] the permittivity of silicon is $\epsilon_{\text{Si}} = 11.7$,^[9] and the permittivity of polyimide is $\epsilon_{\text{PI}} = 3.5$.^[20]

It is well known that LP and CP waves can be written in the form of Equations (1)–(3) in the form of LP EMWs along the x and y directions, and left-handed and right-handed circular polarization (LCP and RCP) EMWs, respectively. After a series of mathematical operations, it can be seen that if Equations (2) and (3) are added together, and if equal amplitudes are assumed, an LP wave of the form Equation (4) holds.

$$\begin{aligned} E_x &= \bar{x}E_x \cos(\omega t + \phi_x - kz) \\ E_y &= \bar{y}E_y \cos(\omega t + \phi_y - kz) \end{aligned} \quad (1)$$

$$\begin{aligned} E_{\text{LCP}} &= E e^{\bar{y}(\omega t + \phi)} \\ &= E [\bar{x} \cos(\omega t + \phi_L) + \bar{y} \sin(\omega t + \phi_L)] \end{aligned} \quad (2)$$

$$\begin{aligned} E_{\text{RCP}} &= E e^{-\bar{y}(\omega t + \phi)} \\ &= E [\bar{x} \cos(\omega t + \phi_R) - \bar{y} \sin(\omega t + \phi_R)] \end{aligned} \quad (3)$$

$$E_{\text{LCP}} + E_{\text{RCP}} = E_{\text{LP}} \cos(\omega t + \phi_{\text{LP}}) \quad (4)$$

To further aid understanding of the process, **Figure 2** displays the synthesis of RCP and LCP waves: as shown in the figure, the RCP wave is rotated in a counterclockwise direction and the LCP wave is rotated in a clockwise direction, taking the angle with the positive direction of the x -axis as ϕ , then at the initial moment, if the appropriate coordinate axis is chosen (e.g., the angle bisector of the two vectors is chosen as the y -axis in the figure), it is easy to know that the vectors are synthesized as a LP wave (polarization along the y -axis in **Figure 2**), and this conclusion does not depend on the initial phase difference.

To further measure the performance of the MFD, the reflected wave and absorptivity A is defined as follows: let the incident wave E_{in} be an LCP wave [Equation (5)], then the reflected wave E_{ref} can be written as Equation (6) of the form where the reflection coefficients for the copolarization ($r_{\text{L-L}}$ and $r_{\text{R-R}}$) and cross-polarization ($r_{\text{L-R}}$ and $r_{\text{R-L}}$) are as in Equation (7). Ideally, there is no significant difference between the reflection coefficients of LCP and RCP waves, so this is not repeated. Based on the above equation, the AR of the reflected wave is Equation (8), which is the ratio of the long axis to the short axis of the ellipse. Equation (9) gives the

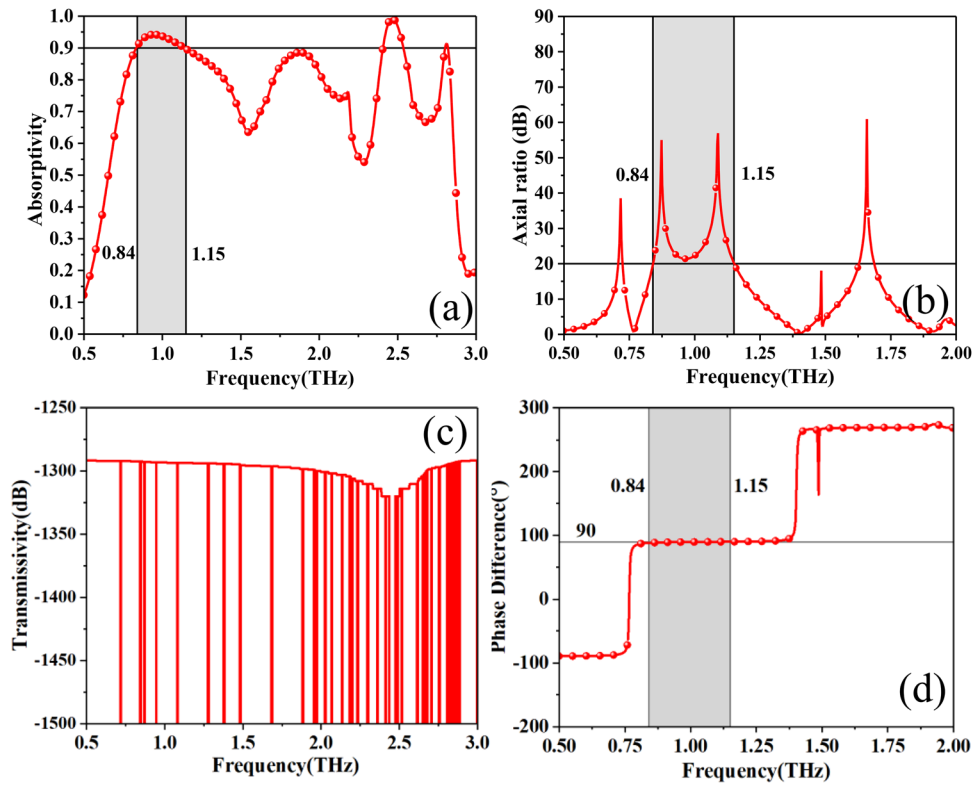


Figure 3. Simulation curves for Structure 1: a) absorption performance, b) AR of reflected waves in PC function, c) transmittance, and d) phase difference in horizontal and vertical directions in PC function.

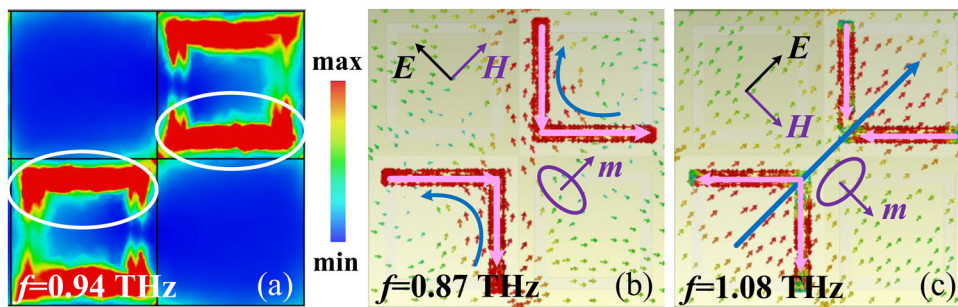


Figure 4. a) Energy density diagram at 0.94 THz, b) surface current diagram at 0.87 THz, and c) surface current diagram at 1.08 THz.

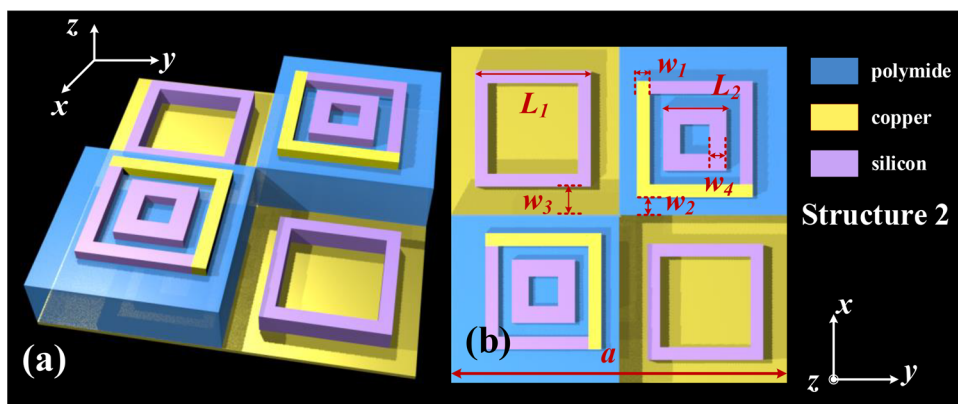


Figure 5. Structure 2 in a) perspective view and b) top view.

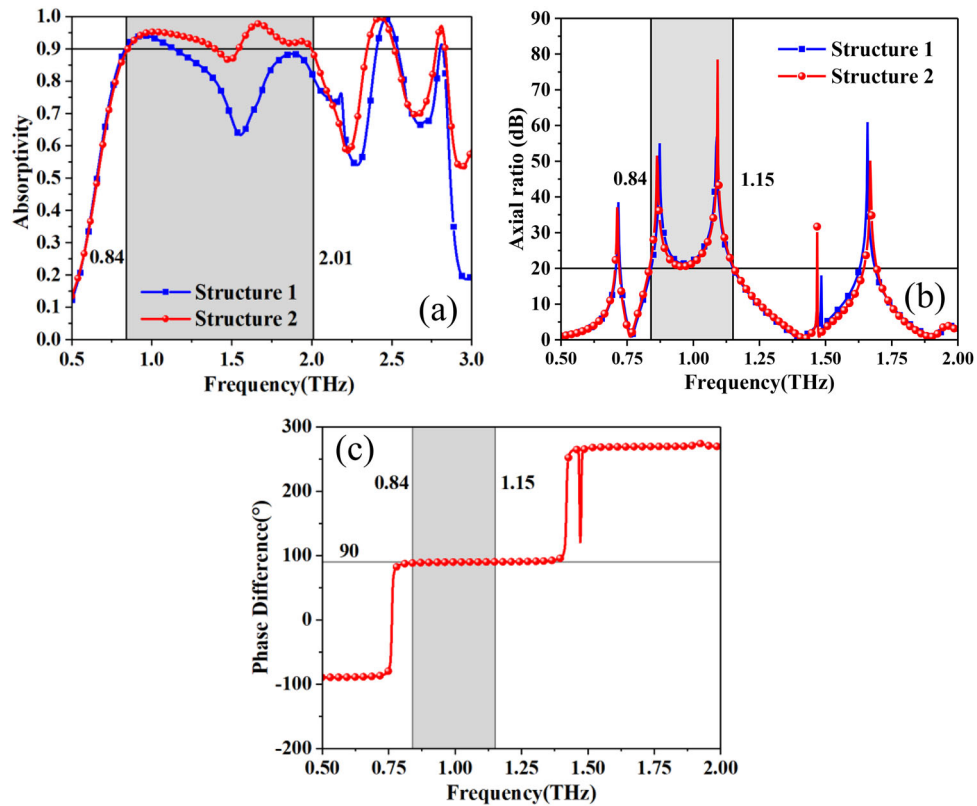


Figure 6. Comparative performance diagrams for Structures 1 and 2: a) absorption, b) AR, and c) phase difference.

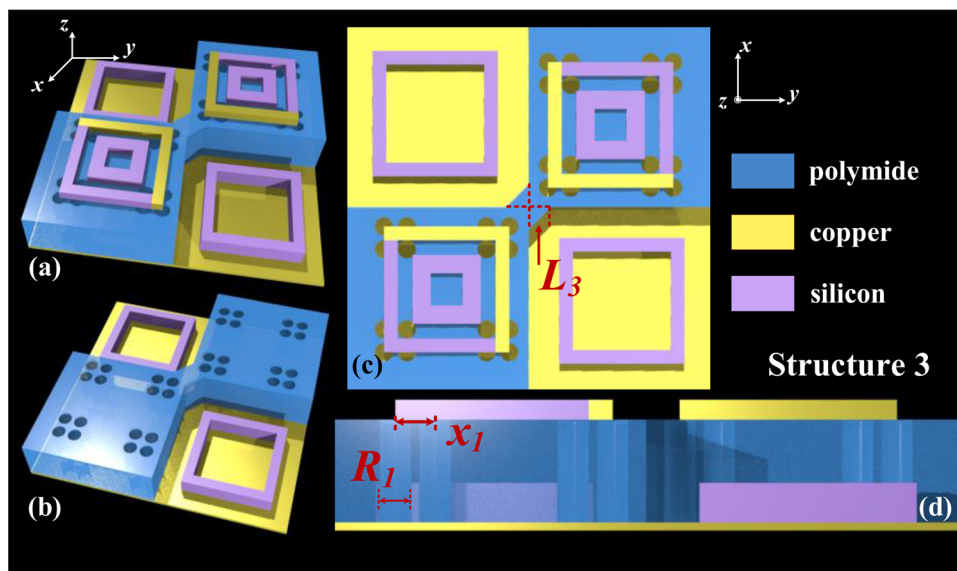


Figure 7. a) Perspective view of Structure 3, b) schematic diagram of the position of the resonant cavity, c) top view, and d) side view.

calculation of the absorptivity A , where $R = |r_{L-L}|^2 + |r_{R-L}|^2$ is the reflectivity and T is the transmissivity. For broadband absorbers, the overall absorption capacity of the operating range can be characterized by the average absorbance, defined by Equation (10) is given, where f represents the frequency.

$$E_{in} = E_{LCP} e^{-j(\omega t + \phi)} \quad (5)$$

$$E_{ref} = \begin{bmatrix} r_{L-L} & r_{L-R} \\ r_{R-L} & r_{R-R} \end{bmatrix} \begin{bmatrix} E_{LCP} \\ E_{RCP} \end{bmatrix} \quad (6)$$

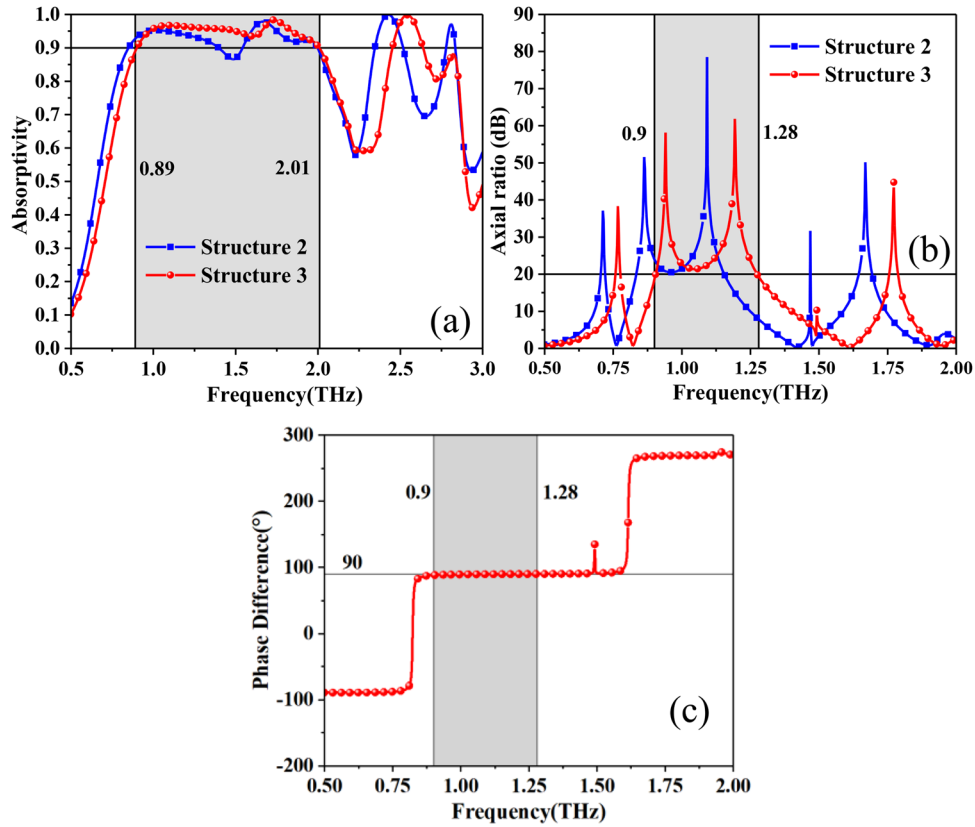


Figure 8. Comparative performance diagrams for Structures 3 and 2: a) absorption, b) AR, and c) phase difference.

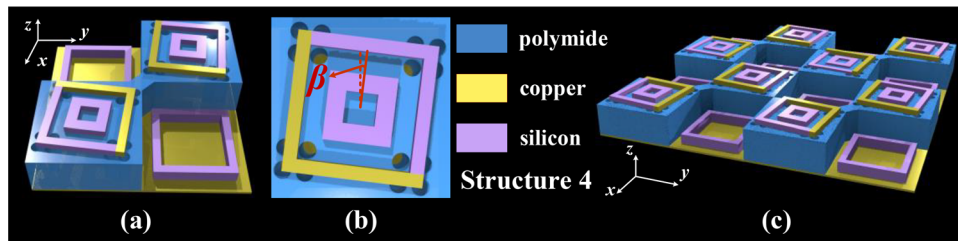


Figure 9. Schematic view of the rotation operation: a) perspective view, b) top view, and c) array structure at work.

$$r_{L-L} = \frac{|E_{LCP}^{ref}|}{|E_{LCP}^{in}|} r_{L-R} = \frac{|E_{LCP}^{ref}|}{|E_{RCP}^{in}|} \quad (7)$$

$$AR = \frac{|E_{LCP}| + |E_{RCP}|}{||E_{LCP}| - |E_{RCP}||} \quad (8)$$

$$A = 1 - R - T \quad (9)$$

$$\bar{A} = \frac{\int_{f_{min}}^{f_{max}} A(f) \cdot df}{f_{max} - f_{min}} \quad (10)$$

All simulation results in this paper are given by HFSS and calculated using the finite element method. After simulation, the performance of Structure 1 in both states is obtained as indicated in **Figure 3**. It can be seen that the absorption performance reaches more than 90% in the range of 0.84–1.15 THz,

and the reflected wave under the PC function in the same frequency reaches an AR of more than 20 dB, so this elliptical polarization wave with a great AR can be taken as an LP wave. As can be seen in **Figure 3c**, T is below -1275 dB in both states, so T can be approximated as 0. **Figure 3d** gives the phase difference between the horizontal and vertical directions in the polarization state, which has excellent dispersion performance for signals of different frequencies as it is constant in the operating band.

To provide a schematic explanation of the above phenomena, **Figure 4a** shows the energy density profile of the absorbed state at 0.94 THz, and **Figure 4b,c** shows the surface current profiles of the PC state at 0.87 and 1.08 THz. When the device is absorbing, the conductivity of the silicon is at 9000 S m^{-1} , allowing the impedance of the entire MFD to match the free space, enabling the EMWs to enter the device, after which the resonance is formed by the square ring made of copper and silicon on the

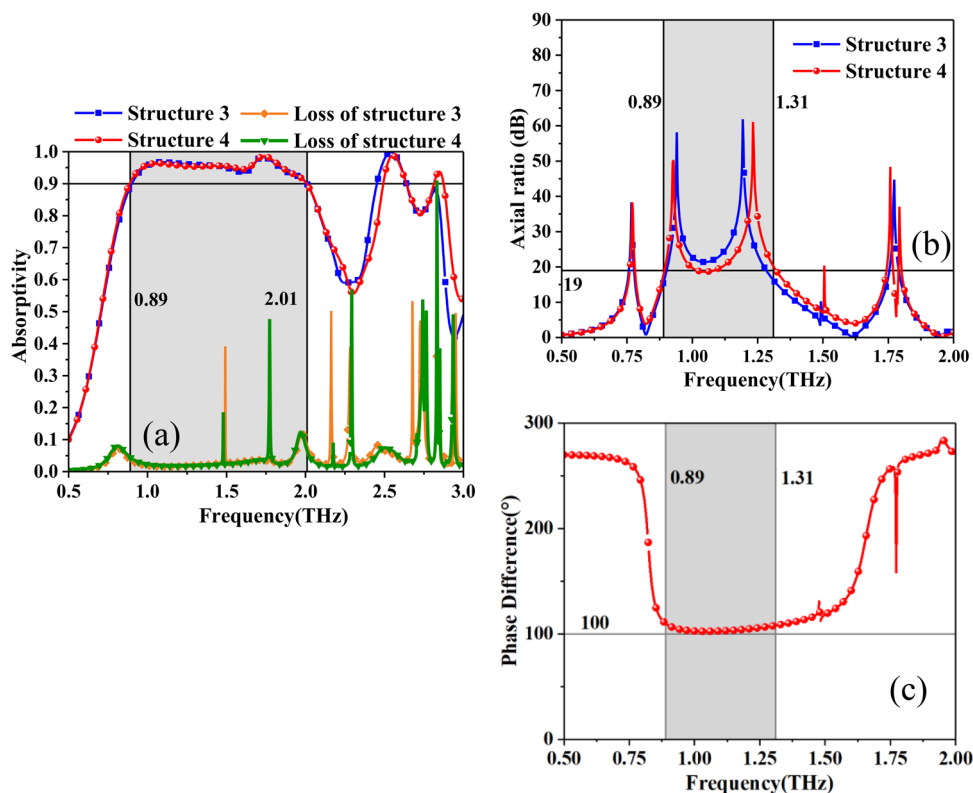


Figure 10. a) Absorptivity of the absorbing state and loss of the PC state, b) AR of the PC state, and c) phase difference of the PC state.

top layer for the loss of the EMWs. As a result, in Figure 4a the energy is concentrated where the ring is located. Figure 4b,c displays the current flow at the two AR peaks in Figure 3b. In the figure, the current flow on the surface of the copper fold on the top layer is marked with pink arrows, while the blue arrows mark the current on the bottom copper plate. It is easy to see that the currents flow in opposite directions at the top and bottom layers in the region of unit B, thus creating a magnetic moment \mathbf{m} and exciting a magnetic field \mathbf{H} , as shown by the purple arrow in the figure, and the changing magnetic field exciting electric field \mathbf{E} . When the amplitude and phase are appropriate, the excited \mathbf{E} combines with the component of the original electric field \mathbf{E}_{in} to form an LCP wave to RCP wave conversion, while unit A reflects the LCP wave as is, after which The reflected RCP wave is superimposed on the LCP wave to form the LP wave, thus forming the CP to LP wave conversion (from the above principle it is clear that if the incident wave is RCP wave, there is no effect on the result).

2.2. Optimizing Absorption Performance

As can be seen from the data given above, there is still very much room for optimization of the absorption curve for Structure 1 in the high-frequency section. Structure 2 is therefore proposed, which adds to the original structure a small concentric square ring at the center of the square ring for enhanced absorption in

the higher frequency band, based on the same mechanism as the external square ring. As illustrated in Figure 5, the width of the added square ring is represented by w_4 , the side length by L_2 , the thickness is the same as the original square ring and the rest of the parameters remain unchanged. A comparison of the performance of Structures 1 and 2 is shown in Figure 6, where the absorption performance is significantly improved, but there is still a hiatus below 90%, while the PC performance remains unchanged.

To increase the absorption rate to over 90% in all operating bands, a set of cylindrical air resonant cavities were added at each of the four corners of the square ring. Structure 3 is displayed in Figure 7, the diameter of the resonant cavities is denoted by R_1 , x_1 is the spacing between the centers of the two cavities, the peripheral cylinders, the centers of which are aligned with the sides of the peripheral ring, and the cavities run through the polyimide. In addition to this, to enhance the losses in the medium, a piece of polyimide is added at the connection of the two units B, half of the diagonal length of which is denoted by L_3 . The remaining parameters are the same as for Structure 2. A comparison of the performance of Structures 3 and 2 is given in Figure 8, where it can be seen that the overall increase in absorption is achieved and the operating band is broadened to achieve ultra-broadband absorption from 0.89 to 2.01 THz with RB = 77%. The PC range, on the other hand, is 0.9–1.28 THz, with little change, just a shift towards higher frequencies, and an RB of 34.9%.

Table 1. Values of the parameters in the structure (μm).

a	L_1	L_2	L_3	t_1
160	62	10	30	2
t_2	t_3	t_4	w_1	w_2
32	5	10	6	17
w_3	w_4	R_1	x_1	β ($^\circ$)
22	8	8	10	7

Table 2. Performance of four structures.

	Absorption band (THz) and RB	PC band (THz) and RB	\bar{A}
Structure 1	0.84–1.15 31%	0.84–1.15 31%	92.5%
Structure 2	0.84–2.01 82%	0.84–1.15 31%	92.9%
Structure 3	0.89–2.01 77%	0.9–1.28 34.9%	95.2%
Structure 4	0.89–2.01 77%	0.89–1.31 38%	95.5%

2.3. Optimizing PC Performance

PC performance can be further optimized by adjusting the position of the two peaks of the AR. Structure 4 is presented in **Figure 9**, where the top pattern of unit B together with the air resonant cavities below is rotated by β degrees in a clockwise direction, the rest of the parameters are the same as in Structure 3. Figure 9c shows the periodic array in operation. The relevant properties of Structure 4 are given in **Figure 10**. In particular, the losses in the PC state are given together in Figure 10a, which does not change significantly compared to Structure 3. In Figure 10b the AR peak at high frequencies is shifted towards high frequencies, eventually achieving a PC of 0.89–1.31 THz and an increase in relative bandwidth to 38%,

Table 3. Comparison with other works.

Refs.	Function	Operating frequency	Performance	Control measure
[7]	Tunable absorption and PC	A: 44–52 THz PC: 11–12.7 THz	RB = 16.7% RB < 15%	Temperature (vanadium dioxide and graphene)
[17]	Dual broadband PC	PC: 5.7–8.62 THz 13.3–15.7 THz	RB = 40% RB = 16.5%	–
[21]	PC and absorption	PC: 2.01–2.56 THz Absorption peak: 1.98 and 3.24 THz	RB = 24% Maximum A = 70.5% or 94.2%	Light (silicon)
[22]	Circular to linear PC	8.34–26.06 GHz	RB = 103%	–
This work	Absorption and PC	A: 0.89–2.01 THz PC: 0.89–1.31 THz	RB = 77% RB = 38%	Light (silicon)

although the lowest AR drops to 19 dB, which is still a very large value and therefore can be considered not to affect performance. In Figure 10c, the phase difference is changed from the original 90° to 100° , which also does not affect the LP wave formation.

3. Results and Discussion

The values of all the parameters in the above structures are given in **Table 1**, and in **Table 2** the performance indicators of the four structures are compared and their average absorption rates are calculated.

To further illustrate the performance of this MFD, a comparison with other works is listed in **Table 3**. From the comparison results, although there exist devices that only implement PC function, which are superior in terms of RB, the proposed MFD has a clear advantage in its class, which combine PC and absorption.

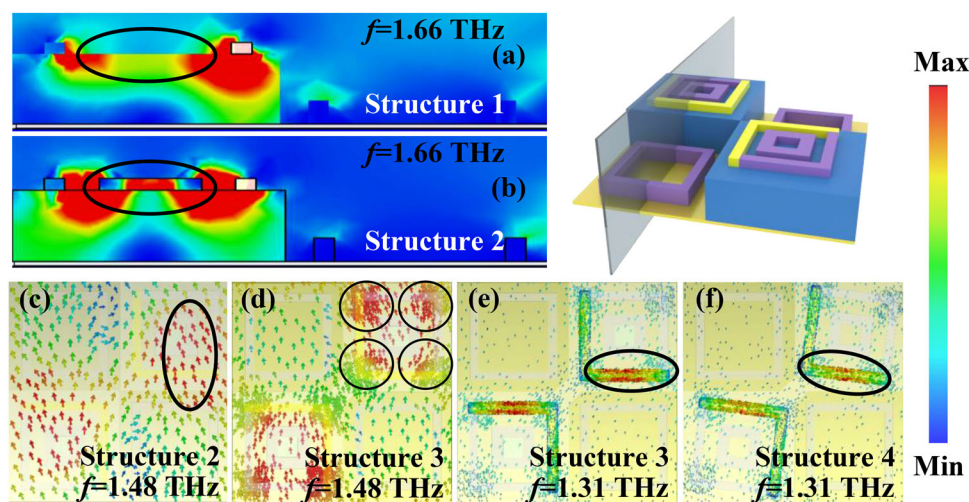


Figure 11. a,b) Energy density distribution diagram for Structures 1 and 2, c,d) bottom surface current diagram before and after the addition of the resonant cavity, and e,f) surface current diagram on the copper folds before and after rotation.

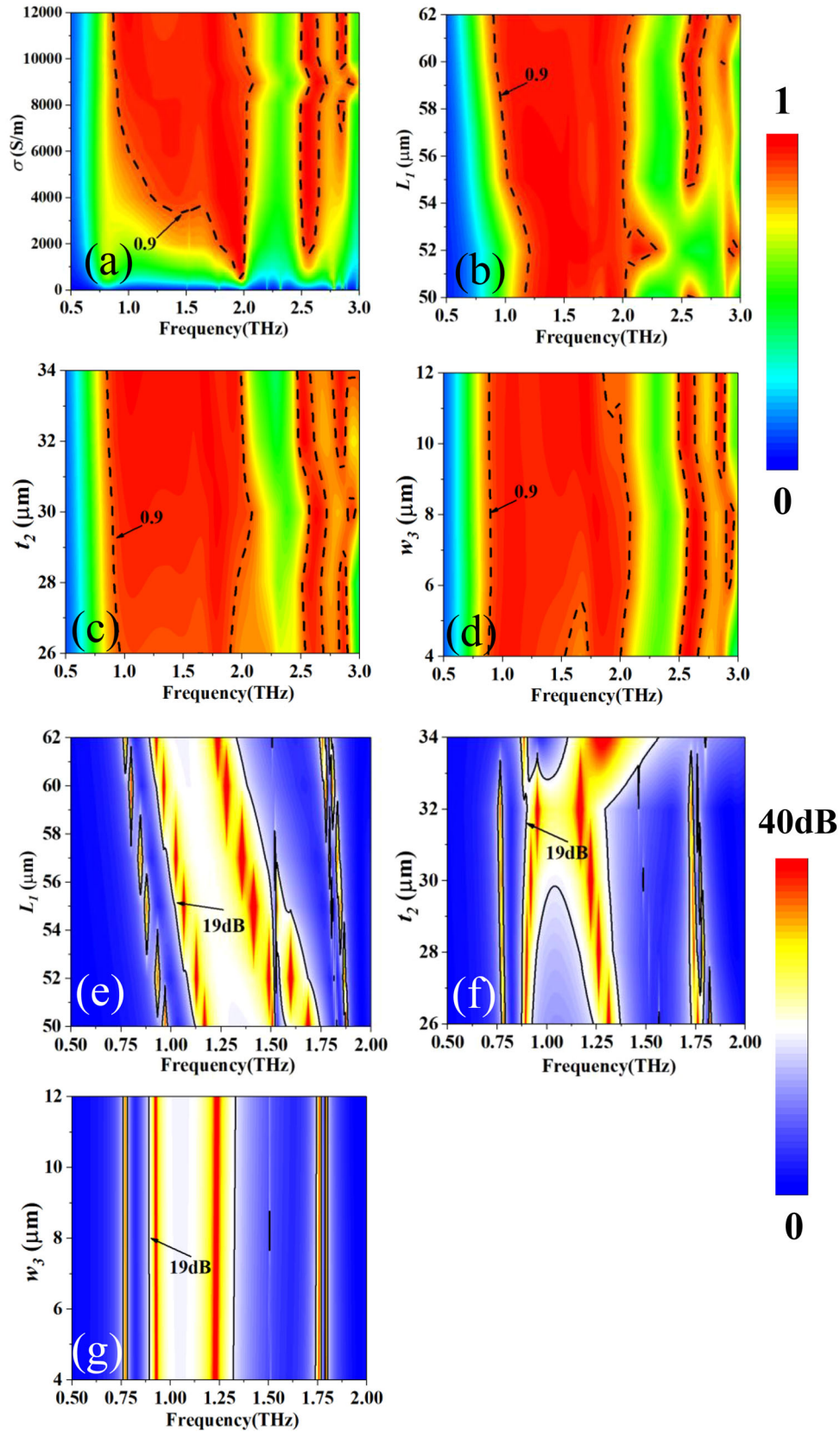


Figure 12. Absorptivity and AR for different parameter values: a) σ , b,e) L_1 , c-f) t_2 , and d,g) w_3 .

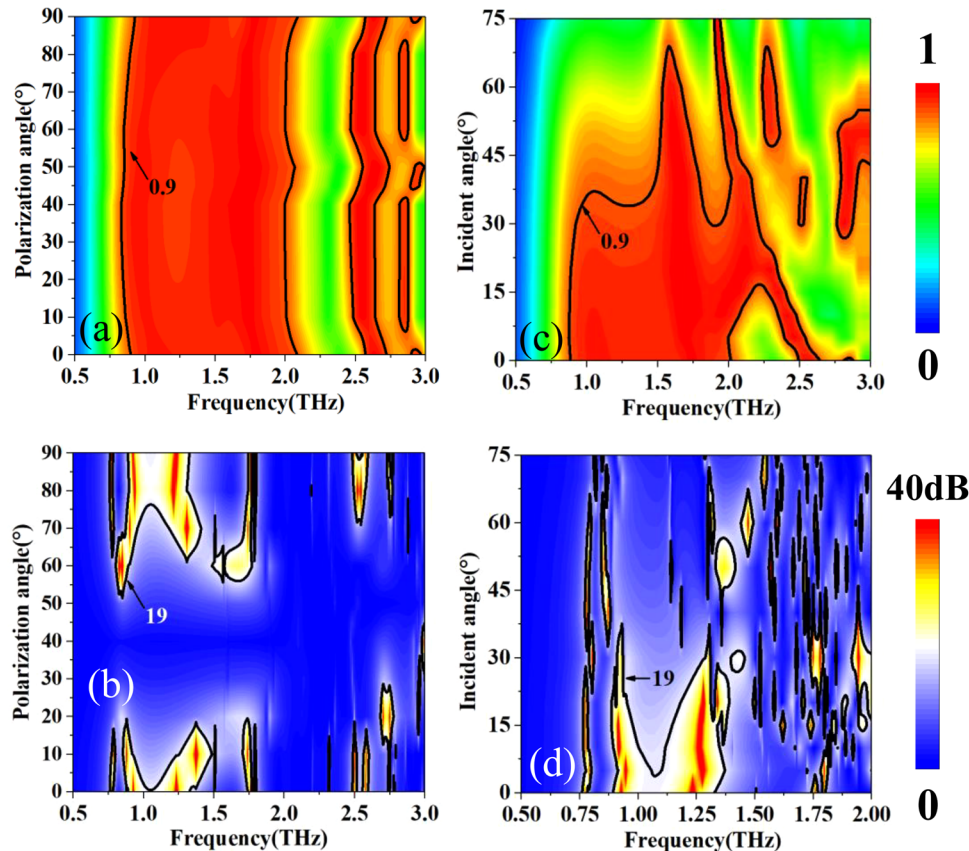


Figure 13. a,c) Performance of absorptivity at different polarization angle and incident angle. b,d) Performance of AR at different polarization angles and incident angles.

3.1. Physical Mechanism

Figure 11 shows the mechanism of the three optimization methods, and the notable places have been marked in the figures. As seen in Figure 11a,b, with the addition of the square ring to the inner ring, the energy density in the central section is significantly enhanced and therefore the resonance in the high-frequency section is significantly enhanced. Figure 11c,d demonstrates the surface currents before and after the addition of the resonant cavity, where the currents are significantly enhanced at the location where the resonant cavity is added, which is responsible for the increased absorption across the operating band. In Figure 11e,f, after the rotational operation, there is a slight weakening of the current in the copper fold, so that the original AR peak is slightly shifted towards the high frequencies, thus widening the PC bandwidth. This is due to the fact that the original symmetrical structure is well coupled at the second AR peak so that almost all of the LCP waves incident are converted into RCP waves, and the LCP waves reflected by unit A are insufficient to match RCP waves into LP waves (The same applies to RCP wave incidence). The rotation operation disrupts the original coupling, shifting the coupling point slightly toward the higher frequencies and therefore widening the bandwidth.

3.2. Parameters Discussion

During the design and optimization process, the performance of the device is most sensitive to changes in the following parameters: conductivity of silicon σ , length of the outer square ring L_1 , the width of the inner square ring w_3 , and the thickness of dielectric layer t_2 . The performance of these parameters at different values is shown in Figure 12. In order to clearly distinguish between absorptivity and AR, two legends are used to represent the different data. As can be seen in Figure 12a, when σ is less than 500 S m^{-1} , absorption is minimal throughout the band and losses can be ignored, at which point it is a PC function. σ is greater than 500 S m^{-1} when more than 90% of the absorption points start to appear, and by 3000 S m^{-1} broadband absorption starts to appear until the maximum bandwidth is reached at $\sigma = 9000 \text{ S m}^{-1}$. Of the remaining parameters, for different w_3 , the absorptivity has a maximum bandwidth, while AR has no effect and is therefore easy to choose. The parameter L_1 , on the other hand, has an absorption bandwidth that grows with increasing values, while AR decreases with increasing values, so the value with the largest absorption region is picked. For different w_3 , AR is hardly affected, so the value with the largest absorption range is selected.

The polarization angle φ and the incident angle θ are also two extremely important parameters. Figure 13a,b shows the

variation of performance with different φ values. It can be noticed that the absorption is relatively stable during the variation, while the AR is extremely sensitive to φ and can form a continuous operating band almost only at $\varphi = 0$. Figure 13c,d gives the performance variation at different θ . The absorption bandwidth is even slightly enhanced at large angular incidence. Again, the AR is very sensitive to θ and only allows θ to vary in the range of 5° .

Meanwhile, the use of parametric inversion can further validate the theoretical results, which can be seen in the Supporting Information.

4. Conclusion

This paper presents an optical control-based MFD that combines the functions of an absorber and a polarization converter, resulting in an ultra-broadband absorption with an average absorptivity of 95.5% (RB = 77%) at 0.89–2.01 THz or a PC from CP to LP waves (RB = 38%) at 0.89–1.31 THz. In addition, three methods for optimizing performance are proposed and the principles are analyzed by energy density diagrams and surface current diagrams. In addition, three methods for optimizing performance are proposed and the principles are analyzed by energy density diagrams and surface current diagrams. Finally, a parametric discussion and parametric inversion are presented. The MFD can be used in the fields of communication, EMW modulation, and electromagnetic shielding.

Supporting Information

Supporting Information is available from the Wiley Online Library or from the author.

Conflict of Interest

The authors declare no conflict of interest.

Data Availability Statement

The data that support the findings of this study are available on request from the corresponding author. The data are not publicly available due to privacy or ethical restrictions.

Keywords

metastructures, multifunctional devices, perfect absorption, polarization converters

Received: April 29, 2023

Revised: May 5, 2023

Published online:

- [1] T. Lin, Y. Huang, S. Zhong, Y. Zhong, Z. Zhang, Q. Zeng, Y. Yu, Z. Peng, *Opt. Lasers Eng.* **2022**, *157*, 107127.
- [2] A. Bhattacharya, R. Sarkar, G. Kumar, *iScience* **2022**, *25*, 103708.
- [3] J. W. Kima, G. H. wang, S. J. Lee, S. H. Kim, S. Wang, *Mech. Syst. Signal Process.* **2022**, *179*, 109374.
- [4] M. T. Ahmadi, M. Hesami, M. Rahmani, *ECSJ. Solid State Sci. Technol.* **2022**, *11*, 081015.
- [5] Q. Li, Z. Tian, X. Zhang, N. Xu, R. Singh, J. Gu, P. Lv, L. B. Luo, S. Zhang, J. Han, W. Zhang, *Carbon* **2015**, *90*, 146.
- [6] H. Jeong, Y. Cui, M. M. Tentzeris, S. Lim, *Addit. Manuf.* **2020**, *35*, 101405.
- [7] M. Mao, Y. Liang, R. Liang, L. Zhao, N. Xu, J. Guo, F. Wang, H. Meng, H. Liu, Z. Wei, *Nanomaterials* **2019**, *9*, 1101.
- [8] L. Liu, L. Kang, T. S. Mayer, D. H. Werner, *Nat. Commun.* **2016**, *7*, 13236.
- [9] Y. Cheng, J. Liu, F. Chen, H. Luo, X. Li, *Phys. Lett. A* **2021**, *402*, 127345.
- [10] S. Zhuang, X. Li, T. Yang, L. Sun, O. Kosareva, C. Gong, W. Liu, *Micromachines* **2022**, *13*, 1239.
- [11] B. Tang, Y. Rena, *Phys. Chem. Chem. Phys.* **2022**, *24*, 8408.
- [12] X. Wang, R. Liu, K. Zhang, R. Liu, J. Zhu, X. Tian, C. Tan, *RIO* **2022**, *9*, 100274.
- [13] N. I. Landy, S. Sajuyigbe, J. J. Mock, D. R. Smith, W. J. Padilla, *Phys. Rev. Lett.* **2008**, *100*, 207402.
- [14] G. Zhao, S. B. M. Niu, Y. Cui, *Mater. Today Commun.* **2019**, *21*, 100603.
- [15] L. Guo, X. Ma, Z. Chang, C. Xu, J. Liao, R. Zhang, *J. Mater. Res. Technol.* **2021**, *14*, 772.
- [16] Z. Xu, R. Gao, C. Ding, L. Wu, Y. Zhang, D. Xu, J. Yao, *Opt. Commun.* **2015**, *344*, 125.
- [17] D. Yang, H. Lin, X. Huang, *Prog. Electromagn. Res. Lett.* **2016**, *61*, 71.
- [18] W. Li, S. Xia, B. He, J. Chen, *IEEE Trans. Antennas Propag.* **2016**, *64*, 5281.
- [19] A. S. Dhillon, D. Mittal, E. Sidhu, *Optik* **2017**, *144*, 634.
- [20] O. Ayop, M. K. A. Rahim, N. A. Murad, H. A. Majid, *Appl. Phys. A* **2014**, *117*, 651.
- [21] D. Yu, Y. Dong, Y. Ruan, G. Li, G. Li, H. Ma, S. Deng, Z. Liu, *Crystals* **2021**, *11*, 1116.
- [22] B. Lin, W. Huang, J. Guo, Y. Wang, Z. Liu, H. Ye, *Opt. Commun.* **2022**, *529*, 129102.